PAPER • OPEN ACCESS

Statistic and Coherence Response of Ship-based Lidar Observations to Motion Compensation

To cite this article: Christiane Duscha *et al* 2020 *J. Phys.: Conf. Ser.* **1669** 012020

View the article online for updates and enhancements.

Recent citations

- An evaluation of surface meteorology and fluxes over the Iceland and Greenland Seas in ERA5 reanalysis: The impact of sea ice distribution
I. A. Renfrew *et al*

Statistic and Coherence Response of Ship-based Lidar Observations to Motion Compensation

Christiane Duscha[1], Mostafa Bakhoday Paskyabi[1], Joachim Reuder[1]

[1]Geophysical Institute, Bergen Offshore Wind Center, University of Bergen and Bjerknes Centre for Climate Research, Postbox 7803, 5020 Bergen, Norway

E-mail: `christiane.duscha@uib.no`

Abstract. Ship-based profiling Lidar systems experience a strong influence of rotational and translational motion on beam direction and hence the line-of-sight velocity. This motion error is inherited by the retrieved 3-dimensional wind vector and is especially visible in the velocity spectra and cross-spectra of velocities at different measurement heights (coherence). Applying motion compensation on the line-of-sight velocity observations was found to have a strong impact on the statistical properties of the retrieved wind vector and successfully improved the corresponding velocity distributions. The impact of motion correction on the spectra of the horizontal wind speed components was found to be neglectable. The Lidar measurement principle, in particular the effect of cross-contamination at higher frequencies, was found to have a larger impact in shaping the horizontal spectra than motion correction. Vertical velocity spectra were strongly affected by ship motion and the motion correction was only partly successful. Precisely, this effect was present at frequencies larger than the resonance frequency of the ship.

1. Introduction

The rotor diameter of state-of-the-art and future planned offshore wind turbines is increasing rapidly, now already exceeding 200 m. Nowadays, most wind power production and turbine load estimates are mainly based on the extrapolation of mean wind characteristics from lower levels, utilizing either the simple wind shear exponent approach or the more advanced Monin-Obukhov similarity theory (MOST)[1]. However, these methods are only applicable within the surface layer, i.e. the lowest part of the atmospheric boundary layer, and in addition only under certain stability conditions [2]. Yet, at the length scale of these new wind turbines, it is not given that these assumptions are valid over the whole rotor diameter. It was found, that assimilating atmospheric observations, such as wind shear, turbulence and atmospheric stability significantly improves both the quality of power production and risk estimates from physical models as well as from statistical models, which are based on machine learning [3].

Unfortunately, the availability of the corresponding marine boundary layer observations is still sparse. Only few platforms featuring meteorological masts (e.g. the FINO platforms in the North and Baltic Sea [4]) or buoy mounted Lidars [5] are installed today. A novel approach to gain detailed observations of wind speed profiles over a larger spacial extend was presented by Gottschall et al. 2018 [6]. They utilized a profiling Lidar on a ferry route over the baltic sea to sample different wind and boundary layer parameters in order to validate the New European Wind Atlas (NEWA) [7]. Similar and accessible ferry infrastructures exist in many coastal

regions interesting for offshore wind exploration. In the future, these might be utilized as a network of mobile wind profile observatories, when equipped with profiling Lidar.

Platforms at sea, e.g. buoys, are exposed to the transfer of momentum from the underlying wave field, causing the platform and the installed Lidar system to move. Here, six degrees of freedom have to be considered, namely the rotational motions around the three main axes, defined as *pitch*, *roll* and *yaw*, and the translational motion along those axes defined as *heave*, *sway* and *surge*. Additional translational motion is generated, if the lidar is installed on a ship for example. Both, wave induced and ship induced motion, influences thus the observation of a ship mounted Lidar.

The following study evaluates the potential of ship-based Lidar installations, with focus on the impact of motion and motion compensation on the Lidar observations. The manuscript is structured as follows. Section 2 describes the measurement campaign, the instrumentation and its limitations used in this study. Section 3 introduces the measurement and retrieval principle, the motion correction algorithm and the data analysis methodology. The main results on statistical, spectral and coherence impact of motion compensation are presented and discussed in Section 4, followed by some concluding remarks in Section 5.

2. Measurements and Instrumentation

2.1. Campaign

The data evaluated in this study originates from the Wincube V2 Lidar observations (see Section 2.2) during the Iceland Greenland Seas Project [8]. During the 7 weeks of the campaign (Feb-Mar 2018), the Lidar was installed on deck (stern side) of the NATO Research Vessel *Alliance*. For the period of the Lidar deployment, the *Alliance* travelled the Iceland and Greenland Seas area, featuring a large range of wind, wave and atmospheric stability conditions. The main part of the cruise was performed at large distance to shore and is therefore representative for offshore conditions. A great advantage of this campaign was the extensive availability of an additional remote sensing and in situ observations. Specifically important boundary layer variables at different heights, such as temperature, humidity and wind were obtained from Radiosonde launches (in situ). This enabled the classification of the data, for example by stability conditions as well as a validation of the remote sensing observations.

2.2. Windcube V2 Lidar Wind Profiler

The Windcube V2 system, manufactured by *Leosphere*, consists of two main parts: a pulsed doppler Lidar and an Inertial Motion Unit (IMU). The pulsed doppler Lidar performs a four beam doppler beam swinging (DBS) scanning pattern (0°, 90°, 180°, 270°) that includes an additional vertical beam (V). A whole cycle of 5 beams corresponds to a duration of approximately 3.8 s (0.72 s for each DBS and 0.97 s for the vertical beam). Along each beam, or line-of-sight (LOS), the Lidar measures radial velocities ($\overrightarrow{v_r}$), obtained from doppler shift of the back-scattered Lidar signal. The three dimensional wind vector $\overrightarrow{u}$ can be retrieved by combining subsequent measurements of $\overrightarrow{v_r}$ (see Section 3.1). The wind vector is obtained at twelve range gates between 40 m and 290 m, with a gate width of 20 m between the lower levels and 30 m between the four highest levels.

When installed on a moving platform at sea (e.g. a ship), the IMU integrated within the Windcube V2 system can be used to obtain motion angles, motion velocities and translational horizontal velocity of the instrument. These parameters are retrieved from internal processing with a frequency of 10Hz. Motions cause the Lidar to observe $\overrightarrow{v_r}$ in a moving coordinate system, that is rotated relative to the earths coordinate system. A basic retrieval (see Section 3.1) in the earths coordinate system, based on this modified $\overrightarrow{v_r}$ will yield incorrect results of three dimensional wind speed. Angular displacement causes exchange of absolute velocity between the different wind speed components. Motion velocities modulate the wind speed components

along the same axis. Finally, translational motions cause a modulation of the horizontal wind speed, depending on the platform heading relative to the wind direction.

2.3. Instrument Limitations with regard to Turbulence

In this study, we will eventually evaluate the impact of motion compensation on the velocity spectra of the wind components, retrieved from Lidar observations. However, general limitations of doppler swinging and profiling Lidar, which are not in motion must be recalled first. In the past, Sathe et. al 2011 [9] found that these kind of Lidar do not perform well in observing turbulence by evaluating 2nd order statistics. Comparisons of Lidar and Sonic spectra (e.g. [10], [11]) found only poor agreement when a certain frequency range was exceeded. Keberlau and Mann 2019 [12] evaluated the main causes for this erroneous spectral behaviour. They concluded that cross-contamination of the horizontal velocity components due to large separation distances of the beams is the dominant source for errors, that is visible in the spectrum. They identified resonance frequencies for eddies corresponding to $2/n$ times the size of the spacial separation distance between the beams ($n = 1, 2, ...$). Secondary sources of contamination were identified from time averaging effects: beams in one complete scanning pattern are used multiple times during the retrieval (see Section 3.1). Retrieved values are therefore not independent from one another, causing a "running mean" effect at frequencies larger than the sampling frequency of the complete scan (~ 3.8s). Additionally, the LOS averaging effect can influence the spectrum and is mainly present at higher frequencies.

3. Methodology

3.1. Lidar Measurement Principle and Basic Retrieval

In its inertial state (no motion), radial velocities measured by the Lidar can be linked to the 3D wind speed vector $\overrightarrow{u}$ following [13] (adjusted for Windcube V2 system):

$$v_r(\theta, \varphi) = u \cdot \sin(\varphi)\sin(\theta) + \text{v} \cdot \cos(\varphi)\sin(\theta) + \text{w} \cdot \cos(\theta) \tag{1}$$

with φ as the azimuth angle and θ as the cone angle of the DBS pattern ($\theta = 28°$). Setting in φ and θ corresponding to the five beams of $\overrightarrow{v_r}$ yields an equation system, that can be solved analytically for $\overrightarrow{u} = (u, v, w)$:

$$u = \frac{v_r(28°, 90°) - v_r(28°, 270°)}{2 \cdot \sin(\theta = 28°)} \qquad v = \frac{v_r(28°, 0°) - v_r(28°, 180°)}{2 \cdot \sin(\theta = 28°)} \qquad w = v_r(\theta = 0°) \tag{2}$$

It should be noted, that unlike the conventional meteorological definition, w is negative defined for upwards directed velocities within the Windcube V2 coordinate system.

3.2. Lidar Motion Compensation

In order to gain motion independent observations of the wind vector, it is possible to apply motion correction to the observations of the Windcube V2 system. The challenge is to compensate for the complex interaction between rotation of the platform's coordinate system and translational and heave motion.

In this study, two simple motion correction methods, introduced by Wolken-Möhlmann et al. 2014 [14], are tested. The computational cheaper method of the two applies motion correction to the retrieved wind vector $\overrightarrow{u_r}$ (see Section 3.1). Here, $\overrightarrow{u_r}$ is rotated corresponding to the motion angles, utilizing the inverse rotation matrix $\mathbf{R}^{-1}$ (for details on $\mathbf{R}$ and its limitations see [15]) and the ship velocity vector $\overrightarrow{u_{ship}}$ is simply subtracted. A disadvantage of this method is, however, that motion correction due to angular displacement and translational and heave motion are decoupled. Additionally, the retrieved wind vector will always be dependent on the

radial velocity observations corresponding to different time steps. Hence, the choice of time step corresponding to the motion data (10Hz resolution) will not sufficiently cover all utilized radial velocity observations ($\sim$ 3.8s).

A possible approach for improvement is to apply the motion correction already on $\overrightarrow{v_r}$ or "pre-retrieval" (also see [14]). A shortcoming of this method is, however, a higher computational cost. For this method, $\overrightarrow{u_{ship}}$ is projected on to the vector along the LOS of each of the Lidar beams. This vector is then subtracted from $\overrightarrow{v_r}$. The resulting motion velocity compensated radial velocity vector $\overrightarrow{v_{rc}}$ can be expressed in terms of the rotated (utilizing $\mathbf{R}$) and LOS projected, three dimensional wind vector. The resulting equation system is, however, not as trivial to solve, as the one introduced in Section 3.1. In order to solve this equation system, linear regression, based on a least squares approach is utilized, following [16].

3.3. Statistic, Spectral and Coherence Analysis

To evaluate the overall quality of the corrected wind speed profile series, it is compared (consistency check) to in situ wind speed measurements that are obtained from 86 Radiosonde ascents, over the course of the cruise at the different Lidar levels. Here, two common error metrics between Lidar and Radisonde data are used: the systematic error (BIAS) and the random or standard deviation error (SDE).

To evaluate the impact of motions on the statistics of Lidar wind observations, a histogram (distribution) of horizontal wind speed and vertical wind speed are created, both for corrected and original series. For more insight on the specific impact of motion velocity on the horizontal wind, an additional histogram of the difference between the corrected and the original horizontal wind speed is estimated, which is conditioned by present and non-present ship translational movement.

For the spectral analysis, the energy spectra of the three wind components, rotated in wind direction (along wind u, cross wind v and vertical wind w) at one level are investigated. Additionally, the cross-correlation spectra between observations of the Lidar at different levels and vertical motion velocity (heave) are evaluated in terms of corresponding coherent modes at specific frequencies. The coherence estimates are constructed from the cross spectral density G_{xy} (and its complex conjugate G'_{xy}), which is the Fourier transform of the cross-covariance function between the variables x and y [17] (x and y are for example series of velocity observed at two different Lidar levels). The coherence estimates are calculated following [17]:

Coherence estimate C:

$$C_{xy} = \frac{G_{xy} \cdot G'_{xy}}{G_{xx} \cdot G_{yy}} \tag{3}$$

real part of Co-Coherence estimate Co (coincident spectrum):

$$Co_{xy} = \text{Re}\left(\frac{G_{xy}}{\sqrt{G_{xx} \cdot G_{yy}}}\right) \tag{4}$$

imaginary part of Co-Coherence estimate iCo (quadrature spectrum):

$$iCo_{xy} = \text{Im}\left(\frac{G_{xy}}{\sqrt{G_{xx} \cdot G_{yy}}}\right) \tag{5}$$

phase ρ:

$$\rho = \text{atan2}\left(\text{Im}(G_{xy}), \text{Re}(G_{xy})\right) \tag{6}$$

The coincident spectrum determines the contributions to the correlation of x and y at different

frequencies, that are "in phase" (phase: 0° or 180°), while the quadrature spectrum determines those, that are "out of phase" (phase: ± 90°) [17].

For analysis, the spectra corresponding to the three velocity components are each combined as a composite of discrete fast Fourier transformation of several time series slices of 30 min length. Each time slice is shifted by 1 min to the proceeding one, over a period of 6 h. Composites of coherence and corresponding estimates (compare Equations 3-6) are estimated in a similar way. A time period of maximum data availability, stationary wind and motion signal was chosen for the spectral analysis of this study. The requirements for stationary were achieved for periods where the statistical properties, in particular mean μ and standard deviation σ, of the evaluated series were independent of absolute time [17], utilizing thresholds for μ and σ of 0.1 m/s and 0.1°, respectively.

4. Results and Discussion

The following Subsections will evaluate and discuss the impact of motion compensation from three points of view: statistical, spectral and from coherent modes. In the process of analysis it was found that distributions, spectra and coherence are similar for the two motion correction approaches introduced in Section 3.2 in almost all evaluated cases. Hence, in order to increase the readability, results from both approaches are only shown and discussed, in case they differ significantly. Otherwise, only the method that applies motion correction "pre"-retrieval is shown.

4.1. Lidar Profile Assessment

First, the quality of the Lidar observations is evaluated in terms of data availability [%] at each level, displayed in Figure 1a. In the lowest levels (up to 100m), the data availability is very close to 100% for the whole campaign (excluding harbour time). However, at higher levels, a decreasing trend of $\overrightarrow{u}$ data availability with increasing Lidar level can be recognised. With decreasing data availability, also reliability decreases and gaps in the series reduce the quality of spectral analysis.

Before determining the consistency of the evaluated Lidar dataset with independent Radiosonde measurements, we need to discuss the limitations such a comparison implies. Previous studies (e.g. [18]) found that Radiosonde measurements of the horizontal wind speed do not agree well with Lidar observations close to the surface, due to inertia effects during the acceleration and oscillatory motion of the Radiosonde. This superimposed motion naturally reduces the

Figure 1. Lidar data availability with height over whole series (a) and Error estimates E (BIAS and SDE) between the horizontal wind speed of Lidar (ws_L) and Radiosonde (ws_R) from original and corrected series (b).

reliability and accuracy of the Radiosonde measurements close to the ground. However, there is no standardized cut-off height for Radiosonde measurements, as inertia and oscillatory effects are dependent on the environmental conditions during release. Lidar observations do not experience such inertial forcing and were in general found to perform well independent of height in comparison to met masts (see e.g. [19]). Flow distortion around the research vessel, however, evidently influences wind speed observations [20]. This can potentially enhance the inertia effect on the Radiosondes, but also modify the wind field observed by the Lidar at the lowest levels
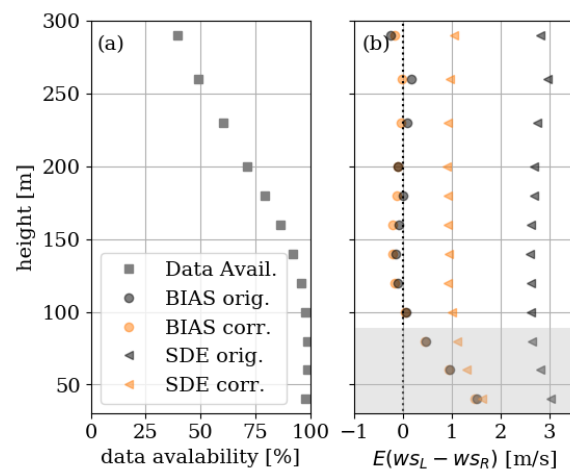
close to the ship.

Direct comparison of the independent datasets displayed in Figure 1b, indeed confirms the observations of previous studies. The systematic differences between Lidar and Radiosonde wind speed are most dominant at the lowest levels. In case of the evaluated campaign, these differences vanish around 100 m for both, the corrected and the original Lidar dataset. In order to avoid potential criticism of "cherry picking" and to make this relevant information available for further deployments, we choose to display the whole profile assessment, but added a shading at the height levels that are critical for the Radiosonde measurements. Still, the strong consistency between Lidar and Radiosonde ws at higher levels, despite the decreased data availability of Lidar data comparable to lower levels, give strong confidence in the Lidar observations.

Even though the systematic differences are very similar between original and corrected ws, a clear improvement of the corrected ws compared to the original ws can be observed in terms of the random differences.

4.2. Statistical Analysis

The original and motion corrected distributions of horizontal and vertical wind speed at the Lidar level corresponding to 100 m are displayed in Figure 2. This level was chosen, because
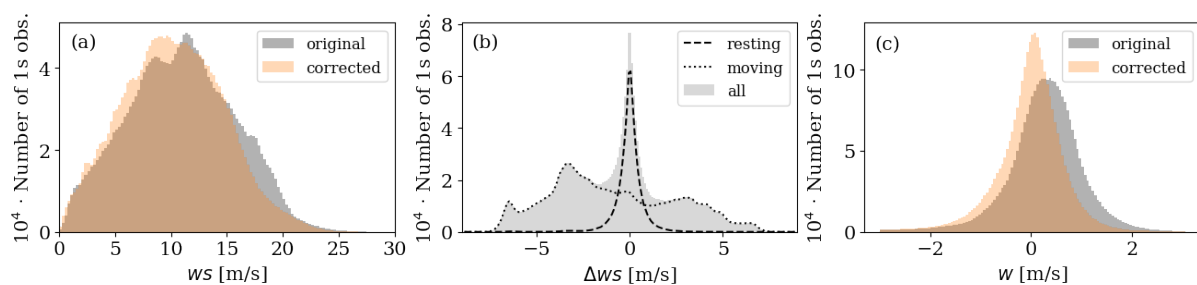

Figure 2. Distribution of original and corrected horizontal wind speed ws (a), distribution of difference between original and corrected horizontal wind speed Δws, conditioned by resting and moving ship (b) and distribution of original and corrected vertical wind speed w distribution.

the most robust results in combined data availability and consistency (Section 4.1) were found at that level.

The distribution of corrected ws (0.25 m/s bin width), shown in Figure 2.a, implies an overall reduction in the amount of observations at higher ws values (between 15 and 20 m/s) in comparison to the original distribution. The amount of observations at lower ws values (between 0 and 15 m/s), on the other hand is increased for almost every bin in this velocity range. The largest impact on the horizontal velocity is expected from ship translational movement (see Section 2.2). If this assumption applies, the adjustment of the ws distribution towards lower ws values after motion correction suggest that the ship was sailing against the mean wind for a longer part of the campaign, or at a higher speed than with the wind.

The distribution of the difference between original and corrected series ($\Delta ws = ws_{corrected} - ws_{original}$) is shown in Figure 2.b. From this distribution (0.1 m/s bin width) a more detailed insight into the cause of adjustment of corrected compared to original ws distribution can be gained. This distribution is conditioned by cases, where the ship was in translational movement and cases, where it was resting at a certain point in space. A distribution of absolute ship speed is shown in Figure 3. As *surge* and *sway* are still larger than zero during periods of rest, translational movement is defined as $u_{ship} > 0.25$ m/s.

The Δws distribution shows a distinct peak around 0 m/s. For resting conditions ($u_{ship} <$ 0.25 m/s) this peak is almost perfectly mapped. Here, maximum and minimum velocity differences vary only around ± 2 m/s. A comparably small portion ($\Delta ws >$ $|0.25m/s|$) of the distribution (resting conditions) can be accounted to the angular motion, meaning a transfer of horizontal velocity to the vertical velocity and vice versa (see Section 3.2). The influence of angular motion on the horizontal wind speed is therefore small in comparison to the overall observed wind speed values. For translational movement conditions ($u_{ship} > 0.25$ m/s), the peak is barely recog-

Figure 3. Distribution of 1 min resolution absolute ship speed $|\overrightarrow{u_{ship}}|$

nisable. For this condition the distribution ranges between -8 m/s to 8 m/s, which is approximately the maximum speed the ship reached within the observation period. This confirms the above formulated hypothesis: ship translational movement can be identified as the dominant motion impact on the originally obtained ws. The amount of negative Δws exceeds the amount of positive Δws. This confirms, that the ship was dominantly sailing against the wind during the evaluated campaign.

For the vertical velocity distributions, which are displayed in Figure 2c, a distinct shift from the original (~ 0.5 m/s) to the corrected (~ 0 m/s) peak velocity value can be observed. The peak additionally narrows after motion compensation. A hypothesis to explain the shift is the dominant presence of a static angular displacement of the Lidar beams. Such an angular displacement causes parts of the horizontal wind speed to be mis-interpreted as vertical velocity and vice versa (see Section 2.2). A reason for displacement could for example be due to imperfectly leveling during installation or a change in ship listing angle over the course of the campaign, e.g. caused by a change in weight distribution by fuel consumption. The hypothesis behind the narrowing of the peak is the successful removal of artificial variance due to a combination of ship angular motion, *heave* motion and non-linear transfer of velocity from the horizontal wind speed components.

4.3. Spectral Analysis

The statistical analysis (Section 4.2) was able to give insight to mean features caused by motion compensation. How and at which frequencies motion compensation is of dominant influence, can on the other hand, be evaluated from original and corrected energy spectra of the three wind components. Figure 4 shows the spectra of those three wind speed components (as defined in Section 3.3) for corrected and original series at the 100 m level. For each spectrum, the frequency range from $1.3 \cdot 10^{-1}$Hz (Nyquist frequency corresponding to one complete scan) and larger frequencies is shaded in grey. At this range, time averaging ("running mean") effects in combination with cross-contamination effects were found to be dominant (see Section 2.3). These effects are visible in all three wind components, but especially in the u and v spectra (Figure 4a & b), in form of a drop in spectral energy at frequencies slightly larger than $1.3 \cdot 10^{-1}$Hz.

Only minor differences between original and corrected spectra of u and v (Figure 4a & b) can be recognised. There is for example slightly less energy in the corrected u and v spectra at the lowest frequencies. A potential explanation for this is the removal of periodic ship movement present during the evaluated period (movement in between periods of resting). Additionally, the corrected v spectrum (Figure 4b) improves slightly in comparison to the original spectrum with respect to the -5/3 slope, characteristic for the inertial subrange of turbulence.
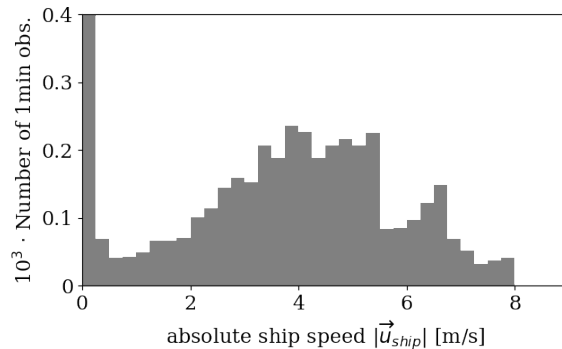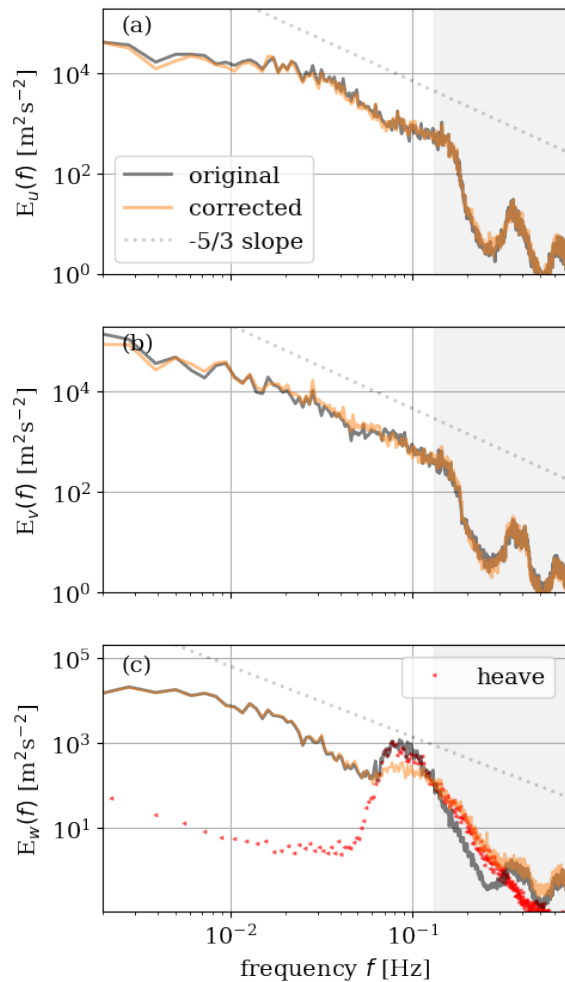
Figure 4. Original and corrected frequency (f) dependent energy spectrum $E_u(f)$ of the along wind component u (a), $E_v(f)$ of the cross-wind component v (b), $E_w(f)$ of the vertical wind speed component w (c). The vertical spectra are accompanied heave spectrum. The grey shading indicates the frequency range which exceeds the Nyquist frequency ($\sim$0.13Hz).

Unfortunately, no in situ measurements of turbulence are available to confirm, that the inertial subrange really is present at this frequency range for the evaluated situation. In contrast to the v spectra (Figure 4b), the slope of both the original and corrected u spectra (Figure 4a) deviates from the -5/3 slope. As this deviation increases with increasing level height and therefore increasing separation distance (see Appendix Figure A1), the cross-contamination effect is most likely responsible for the deviation in slope from the inertial subrange.

In case of the vertical component, the spectra were found to differ in between the retrieval methods introduced in Section 3.2. Both corrected and original spectra of the two retrieval methods are displayed in the Appendix Figure A2. One major difference to point out between the two methods: the spectra corresponding to the "basic" retrieval were found to fit better with the -5/3 slope of the inertial subrange than the "pre"-retrieval method.

In contrast to the u and v spectra, the impact of motion compensation can be identified clearly, when evaluating the w energy spectra, shown in Figure 4c. One advantage in the analysis of the w spectra is, that we also can display *heave* in the same coordinate system (here plotted in red), as it has the same unit $[m/s]$ and direction (z) as w. *Heave* motion results from the ship oscillations, which are forced by the underlying wave field. These oscillations amplify close to the natural frequency specific to the ship. A peak in *heave* spectrum can therefore be related to the resonance frequency of ship and wave field.

A clear peak at $8 \cdot 10^{-2}$Hz can be identified in the original w spectrum, shown in Figure 4c. This peak is maximal at the same frequency and is of similar magnitude as the peak in *heave* spectrum (Figure 4c). However, at frequencies larger than $1.3 \cdot 10^{-1}$Hz, the slope of the original w spectrum is steeper than the slope of the *heave* spectrum. The peak is also observed for the corrected w spectrum, yet it is reduced in comparison to the original w spectrum between $6 \cdot 10^{-2}$Hz and $1.3 \cdot 10^{-1}$Hz. For $f > 1.3 \cdot 10^{-1}$Hz, on the other hand, the spectral energy of the corrected spectrum is increased. At this frequency range it is of similar magnitude and slope as the *heave* spectrum. A hypothesis to explain this behaviour is, that the oscillations caused by motion can not be resolved at this frequency range by the Lidar measurement principle (Section 3.1). If this hypothesis is true, motion compensation possibly caused a transfer of energy, which is conserved in the motion measurement, artificially to the spectral energy of

corrected w. This hypothesis is evaluated utilizing coherence estimates and coherent modes in the following subsection.

4.4. Coherence Analysis

Original and corrected estimates of spectral coherence, real and imaginary part of the co-coherence and the phase between series of w at different Lidar levels are, together with *heave*, displayed in Figure 5. These estimates are in the following utilized to identify coherent modes
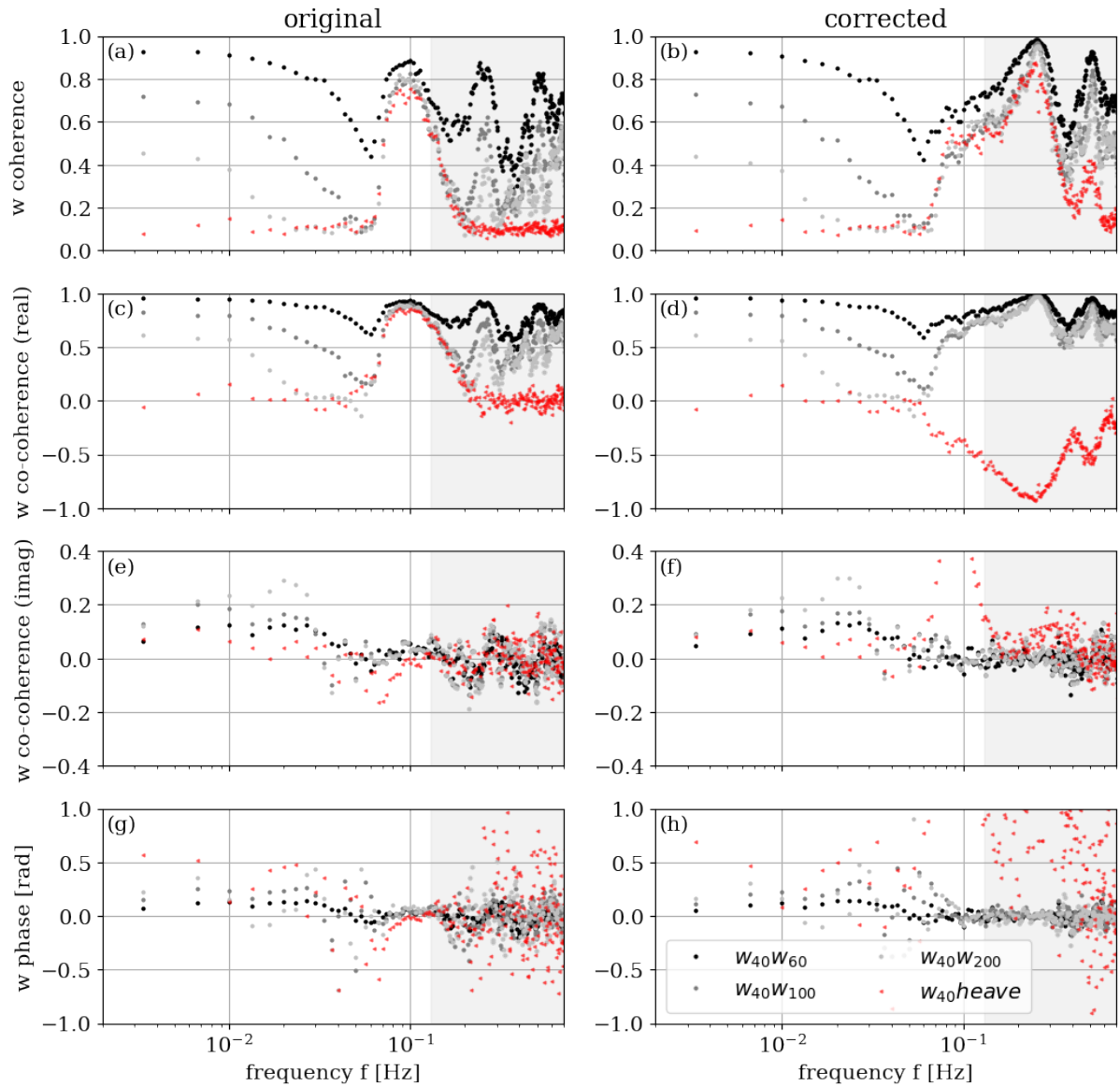

Figure 5. Coherence estimates from cross spectral density estimates of vertical velocity $w_i w_j$ between different Lidar levels ($i = 40m$ and $j = [60m, 100m, 200m]$) and *heave*. Coherence $C_{w_i w_j}$ and $C_{w_i,heave}$ of original w (a) and corrected w (b), real co-coherence $Co_{w_i w_j}$ and $Co_{w_i,heave}$ of original w (c) and corrected w (d), imaginary co-coherence $iCo_{w_i w_j}$ and $iCo_{w_i,heave}$ of original w (e) and corrected w (f) and phase $\rho_{w_i w_j}$ and $\rho_{w_i,heave}$ of original w (g) and corrected w (h).

at specific frequencies, with focus on motion impact.

A turbulent eddy of a specific size s_E ($\sim f$) will be recognised at two different points in space (correlation), if their separation distance is smaller than s_E. Hence, in theory, the spectral coherence of w at two different levels is expected to overall decrease with frequency and vertical separation distance.

From the original spectral coherence estimate shown in Figure 5a, a coherent mode ($6\cdot10^{-2}$ Hz$<$ $f<2\cdot10^{-1}$ Hz) can be identified for all coherence estimates of w_iw_j at two different levels i and j. The maximum of the coherent mode can be identified around 10^{-1}Hz. At a frequency around $6\cdot10^{-2}$Hz, the spectral coherence of w_iw_j ($j = 100m$ and $j = 200m$) decreases to minimal values, then both coherence estimates increase rapidly (to ~ 0.8) and in the same manner, matching the spectral coherence between w and *heave*. This implies that spectral coherence (correlation) at this frequency range is mainly caused by ship motion (around the resonance frequency). At higher frequencies ($f>2\cdot10^{-1}$Hz) the coherent modes can be identified in between w at different levels, but not with *heave*. For this frequency range, the increased spectral coherence between w at different levels is potentially connected to the limitations in the measurement and retrieval principle in combination with cross-contamination at the resonance frequencies (Section 2.3).

Similar, and even more distinct peaks were also identified from coherence estimates of a Lidar, which was installed on a fixed platform. The w coherence estimate from a measurement corresponding to this fixed period is shown in Figure 6.

For all frequencies of the coherent mode, the real part of the original spectral co-coherence (Figure 5c), is positive (correlated). For frequencies around maximum correlation ($\sim 10^{-1}$Hz), the imaginary part of the co-coherence (Fig. 5e) is very close to zero. This implies, that the w series in not only strongly correlated with *heave* and in between the levels for the frequency range of the coherent mode, but also also in phase (phase mode), as shown in Figure 5g.

Figure 6. Spectral coherence between different levels of observations from a Lidar installed on a fixed platform (no motion)

The spectral coherence corresponding to the corrected w series at different levels and with *heave* is shown Figure 5b. In comparison to the original coherent mode with *heave* (Fig. 5a), the corrected coherent mode with *heave* is present over a larger frequency range and at higher frequencies. Within the frequency range of the original coherent mode, the corrected coherent mode is reduced in magnitude. Yet, real corrected spectral co-coherence (Figure 5d) is negative (anti-correlated) and the imaginary corrected spectral co-coherence (Figure 5f) is strongly increased and therefore out of phase (anti-phase mode) at this frequency range (Figure 5h). This implies that the motion correction potentially overcompensates and introduces opposing and out of phase oscillations to the w series. At frequencies larger than the Nyquist frequency (grey shaded), cross-correlation with *heave* and corrected spectral coherence in between the levels increases (Figure 5b). From the real part of the corrected spectral co-coherence (Figure 5d) it can be observed, that the motion correction causes w and *heave* to be anti-correlated as well. Especially for frequencies $> 1.3\cdot10^{-1}$Hz the anti-correlation corresponding to the corrected coherent mode (Figure 5d) is strongly increased in comparison to the original coherent mode (Figure 5c). This supports the hypothesis formulated in Section 4.3: At this frequency range the Lidar observations are not able to resolve oscillations connected to ship motion and motion correction introduces artificial oscillation on the corrected w series.
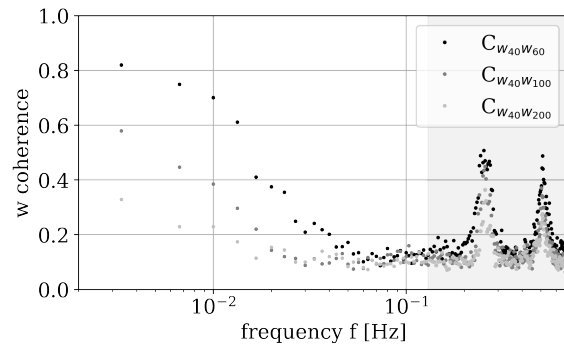
5. Conclusions and Outlook

Motion correction has a strong impact on mean horizontal and vertical wind speed and was found to be able to adjust the analysed series towards more realistic distributions. The impact of motion on spectra of horizontal wind speed components, is found to be small in comparison to limitations caused by the measurement principle, in particular due to cross-contamination. In contrast, the vertical velocity spectrum was found to be strongly impacted by motion contamination. Motion correction is only partly successful. It even causes the series (and spectrum) to be more complicated to separate in a realistic and an erroneous part. On basis of these findings, it is not recommended to utilize a time resolution finer than the time the Lidar system requires for one complete scanning cycle (~3.8 s), even though it can be provided. Specifically for the vertical component, an even smaller part of the spectrum should be considered, depending on the natural frequency of the ship, the Lidar is installed on. In this case, it is recommended to utilize the w component, which is only retrieved from the vertical beam ("basic"), as it is less contaminated by cross-contamination, inherited from the horizontal components.

In order to gain information on turbulence, there exists the possibility to replace the un-resolvable part of the velocity spectra by a theoretical formulation (e.g. the Kaimal spectrum [21]), if it is possible to identify the inertial subrange[1]. Here additional information on stability can for example be used to achieve more realistic spectra. Improved turbulence estimates such as turbulent kinetic energy (TKE) and turbulence intensity can be acquired from integrating the adjusted spectra.

There are also other approaches to correct for motion in turbulence estimates. In order to remove motion impact on momentum flux estimates, Rieder and Smith 1998 [23] suggested a method which utilizes the cross-correlation spectra between velocity components and motion estimates to directly correct cross-correlation spectra between two of the velocity components (momentum flux).

References

[1] Monin, A. S. and A. M. Obukhov, 1954, Basic laws of turbulent mixing in the atmosphere near the ground, Tr. Akad. Nauk SSSR Geofiz. Inst 24 (151), 163-187.

[2] Gryning, S.-E., Batchvarova E., Brümmer B., Jørgensen H., and Larsen S., 2007, On the extension of the wind profile over homogeneous terrain beyond the surface boundary layer, Boundary-Layer Meteorol., 124(2), 251-268, doi:10.1007/s10546-007-9166-9.

[3] Optis M. and J. Perr-Sauer, 2019, The importance of atmospheric turbulence and stability in machine-learning models of wind farm power production, Renewable and Sustainable Energy Reviews, Volume 112, Pages 27-41, ISSN 1364-0321, doi:10.1016/j.rser.2019.05.031.

[4] Fischer G., 2006, Installation and Operation of the Research Platform FINO 1 in the North Sea In: Köller J., Köppel J., Peters W. (eds), Offshore Wind Energy. Springer, Berlin, Heidelberg, doi:10.1007/978-3-540-34677-7-15.

[5] Gottschall, J., Gribben B., Stein D., and Würth I., 2017, Floating lidar as an advanced offshore wind speed measurement technique: current technology status and gap analysis in regard to full maturity, Wiley Interdisciplinary Reviews: Energy and Environment, 6(5), e250, doi:10.1002/wene.250.

[6] Gottschall J., Catalano E., Dörenkämper M. and B. Witha, 2018, The NEWA Ferry Lidar Experiment: Measuring Mesoscale Winds in the Southern Baltic Sea. Remote Sensing, 10 (10), 1620, doi:10.3390/rs10101620.

[7] Karagali, I., Hahmann A. N., Badger M., Hasager C., and Mann J., 2018, Offshore New European Wind Atlas, Journal of Physics: Conference Series, 1037, 052007, doi:10.1088/1742-6596/1037/5/052007.

[8] Renfrew, I. A. et al. , 2019, The Iceland Greenland Seas Project, Bulletin of the American Meteorological Society, Volume 100, Number 9, Pages 1795-1817, https://doi.org/10.1175/BAMS-D-18-0217.1

---

[1] It should be noted that not only motion and cross-contamination effects can contaminate the inertial subrange. Also random waves (wave-induced motions) can modify the slope of the inertial subrange, even for frequencies far from the wave peak [22]

[9] Sathe, A., J. Mann, J. Gottschall, and M.S. Courtney, 2011: Can Wind Lidars Measure Turbulence?. J. Atmos. Oceanic Technol., 28, 853–868, https://doi.org/10.1175/JTECH-D-10-05004.1

[10] Canadillas, B., Bégué, A. and T. Neumann, 2010: Comparison of turbulence spectra derived from LiDAR and sonic measurements at the offshore platform FINO1. 10th German Wind Energy Conference (DEWEK 2010), No. Dewek

[11] Kumer,V. M., Reuder J., Dorninger, M., Zauner, R. and V. Grubisic, 2016, Turbulent kinetic energy estimates from profiling wind LiDAR measurements and their potential for wind energy applications. Renewable Energy, 99, 898 - 910, https://doi.org/10.1016/j.renene.2016.07.014

[12] Kelberlau, F. and Mann, J., 2019, Cross-contamination effect on turbulence spectra from Doppler beam swinging wind lidar, Wind Energ. Sci. Discuss., https://doi.org/10.5194/wes-2019-71, in review

[13] Weitkamp, C., 2005, Lidar: Range-Resolved Optical Remote Sensing of the Atmosphere, Springer Series in Optical Sciences, Vol. 102, Springer, New York, NY, USA

[14] Wolken-Möhlmann, G., Gottschall, J. and Lange, B., 2014, First Verification Test and Wake Measurement Results Using a SHIP-LIDAR System. Energy Procedia. 53. https://doi.org/10.1016/j.egypro.2014.07.223 .

[15] Thwaites, F. T. 1995, Developement of an acoustic vorticity meter to measure shear in Ocean-Boundary Layers, Massachusetts Institute of Technology, https://doi.org/10.1575/1912/1576.

[16] Lai, T. L., Robbins, H. and Wei, C. Z., 1978, Strong consistency of least squares estimates in multiple regression, Proceedings of the National Academy of Science, Volume 75, Pages 3034–3036, ISSN 0027-8424, https://doi.org/10.1073/pnas.75.7.3034.

[17] Emery, W. J. and Thomson, R. E., 2001, Data Analysis Methods in Physical Oceanography, Chapter 5 - Time-series Analysis Methods, Elsevier Science, Pages 371-567, ISBN 9780444507563, https://doi.org/10.1016/B978-044450756-3/50006-X.

[18] Kumer V.M., Reuder J. and Furevik B. R. 2014, A Comparison of LiDAR and Radiosonde Wind Measurements, Energy Procedia,Volume 53, Pages 214-220, ISSN 1876-6102, https://doi.org/10.1016/j.egypro.2014.07.230.

[19] Westerhellweg, A., Canadillas, B., Beeken, A. and Neumann, T., 2010, One year of LiDAR measurements at FINO1-Platform: Comparison and verification to met-mast data, 10th German Wind Energy Conference DEWEK 2010

[20] Yelland, M. J. and Moat, B. I. and Pascal, R. W. and Berry, D. I., 2002, CFD Model Estimates of the Airflow Distortion over Research Ships and the Impact on Momentum Flux Measurements. Journal of Atmospheric and Oceanic Technology, 19, 1477-1499,https://doi.org/10.1175/1520-0426(2002)019¡1477:CMEOTA¿2.0.CO;2

[21] Kaimal, J.C., Wyngaard, J.C., Izumi, Y. and Coté, O.R. (1972), Spectral characteristics of surface-layer turbulence. Q.J.R. Meteorol. Soc., 98: 563-589. doi:10.1002/qj.49709841707.

[22] Lumley, J.L., Terray, E.A., 1983, Kinematics of turbulence convected by a random wave field., J Phys Oceanogr 13:2000–2007

[23] Rieder, K. F. and Smith, J. A. 1998, Removing wave effects from the wind stress vector, J. Geophys. Res., 103(C1), 1363– 1374, doi:10.1029/97JC02571.
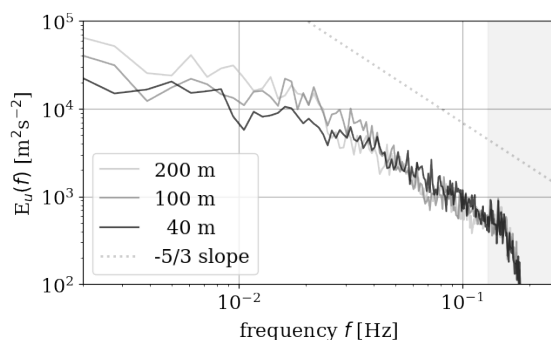
A. Appendix: Figures

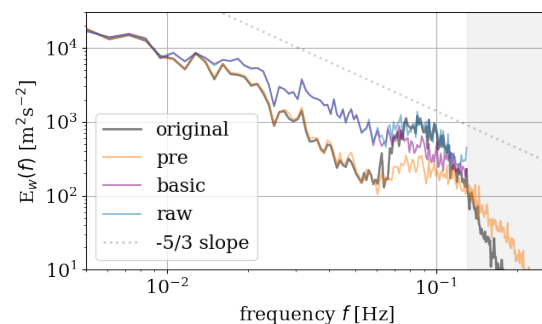**Figure A1.** Along wind (u) energy spectra corresponding to different Lidar level

Figure A2. Vertical velocity (w) spectra, corresponding to different retrieval and motion correction appoaches